Received 31 December 2022; revised 11 January 2023; accepted 17 January 2023. Date of publication 27 January 2023; date of current version 15 February 2023.

Digital Object Identifier 10.1109/OJAP.2023.3240137

Synthesis of 3-D Polarization Rotation Transmissive Surface by Arbitrary Angle Based on Orthogonally Inserted Parallel-Couple Slotlines

TAO WEI [1,2] (Graduate Student Member, IEEE), BO LI [1] (Senior Member, IEEE), HANXUAN LI [1] (Graduate Student Member, IEEE), LEI ZHU [3] (Fellow, IEEE), AND CHONG-HU CHENG [1] (Member, IEEE)

[1]School of Electronic and Optical Engineering, Nanjing University of Posts and Telecommunications, Nanjing 210023, China

[2]School of Information Engineering, Baise University, Baise 533000, China

[3]Department of Electrical and Computer Engineering, University of Macau, Macau, SAR, China

CORRESPONDING AUTHORS: B. LI AND L. ZHU (e-mail: elibo@njupt.edu.cn; leizhu@um.edu.mo)

This work was supported in part by the National Key Research and Development Program of China under Grant 2021YFE0205900; in part by the National Natural Science Foundation of China under Grant 62071243 and Grant 61971475; and in part by the Macau Science and Technology Development (FDCT) Fund under Grant 0085/2020/AMJ and Grant 0095/2019/A2.

ABSTRACT In this article, a polarization rotation transmissive surface (PRTS) of arbitrary angle based on a three-dimensional (3-D) frequency selective structure is proposed. The PRTS unit cell is composed of three parallel-coupled slotline sections with open-short ends etched on vertically and horizontally inserted single-layer printed circuit boards (PCBs). Under the incidence of vertically polarized waves, the spatial waves are converted into guided waves by the open-circuited end of one slotline section, and then the guided waves are coupled to two other slotline sections that can act as two independent coupling transmission paths in the orthogonal planes. This can be observed as a power divider, and the power division ratio can be fully controlled by virtue of the coupling strengths of the two coupling transmission paths. Thus, the polarization of incidence waves can be rotated at an arbitrary angle at the output port. To simplify the design procedure, a filtering power division theory and an equivalent circuit model are first used to obtain the theoretical response. Subsequently, a coupling matrix is employed to synthesize and design the proposed PRTS. To confirm the effectiveness of the proposed PRTS, two examples with different polarization rotation angles and fractional bandwidths at the same center frequency of 5 GHz and return loss of 20 dB are designed, fabricated, and measured. The measured results confirm our theoretical predictions and agree with the simulated results, thus demonstrating that the proposed PRTS exhibits stable frequency response under a large oblique incidence, in addition to their easiness in fabrication.

INDEX TERMS Frequency selective surface (FSS), polarization rotation (PR), slotline, synthesis method.

I. INTRODUCTION

POLARIZATION-ROTATING surfaces (PRSs) are kinds of spatial passive components that can rotate the polarization direction at a certain angle when the incident electromagnetic (EM) waves pass through them. The special structures have been investigated and widely used in multiple applications such as antenna systems [1], imaging radar [2], and modern military stealth radar [3]. As per the propagation direction of outgoing waves, PRSs can be categorized into two primary groups: polarization rotation reflective surfaces (PRRSs) [4], [5], [6], [7], [8], [9], and polarization rotation transmissive surfaces (PRTSs) [10], [11], [12], [13], [14]. Generally speaking, co- and cross-polarized reflection are only considered in PRRSs because the incident EM waves are completely reflected by a perfect conductor set behind PRRSs. However, co- and cross-polarized transmission and co- and cross-polarized reflection are considered in PRTSs, thus resulting in design challenges [15].

Over the past few decades, many studies have been carried out for PRTSs with 90° polarization rotation (PR). Multilayers, including wire grids, have been reported [16], [17], which have the advantages of broadband operation, low insertion, and easy fabrication. Design approaches based on the substrate-integrated waveguide (SIW) cavity technology have been presented [18], [19], [20], which can obtain good frequency selectivity and sharp-roll off skirts at passband edges. However, the large profile of these structures and the fabrication cost consequently limit their practical applications. Recently, structures with double-sided slot resonant [21], [22], or orthogonal capacitive surfaces [23] have been reported and they are typically composed of back-to-back slots or patch resonators coupled via a narrow aperture. These types of PRTSs can provide thin thickness, wideband, and low inserted loss (IL). Whereas these designs are limited because of the large size of the periodic elements, thus resulting in poor angular stability. Moreover, they can only provide 90° PR.

Arbitrary polarization rotators have received considerable attention because they can meet the requirements of different PR angles [24], [25], [26], [27]. A polarization rotator with meander-line grids that allows for the arbitrary rotation of linear polarization has been described [24]. In [25], a polarization rotator of arbitrary angle has been reported, where each unit cell contains double metallic layers etched with a slot. By adjusting the rotation direction of the slot on each layer, the electric field direction can be rotated when penetrating the structure. A waveguide polarization rotator has been used to demonstrate that an arbitrary angle of polarization plane rotation can be obtained by EM-coupling two conjugated quadruple-slot planar–chiral irises [26]. Broadband polarization rotators for rotating arbitrary polarization angles by improved SIW cavities are presented in [27], [28], where the PR can be achieved by controlling the rotation angle of input and output slots etched on two sides of the SIW cavities. Although these above-mentioned PRTSs have the same advantages in terms of design, they suffer from their sensitivity to oblique incidence because they are designed by two-dimensional frequency selective surfaces (2-D FSSs) with high periodicity in transversal cross-section.

In recent years, a class of three-dimensional (3-D) FSSs based on a periodic array of cavity elements has been proposed [29], [30], [31]. Because of the special construction of unit cells, 3-D FSSs can provide multi-mode resonators in the longitudinal direction in the FSS element, thus resulting in high-order filtering response or wideband performance [30]. Furthermore, 3-D FSSs exhibit good angular stability because of the miniaturized transversal size of these 3-D unit cells. More recently, ultra-wideband bandpass 3-D FSSs based on direct synthesis methods have been investigated and designed [32]. Therefore, owing to the operation characteristics of 3-D FSSs, many designs have been proposed [33], [34], [35].

In this article, a novel concept of synthesizing and designing PRTS with arbitrary angles based on 3-D FSSs is presented, which comprises three straight slotline sections with open short ends etched on an orthogonally inserted printed circuit board (PCB). Under the incidence of linearly polarized incident waves in the vertical direction, the spatial waves are converted into guided waves at the open end of one slotline and then coupled to the other two parallel slotline sections etched on the orthogonal PCB. Thus, the combination of the two perpendicular electric fields will be rotated by the two coupling paths at the output port. To reveal this procedure, a filtering power divider concept with an equivalent circuit model is developed to analyze the operating characteristics of the proposed PRTS. Meanwhile, a synthesis method with a coupling matrix is used to design the proposed PRTS. The synthesis and design procedure are then discussed in detail. Two examples with different PR angles and fractional bandwidths at the same center frequency and return loss (RL) are designed. In final, two examples with fractional bandwidths of 20% and 13% with PR angles of 30° and 45° are fabricated and measured, respectively. Good agreement is obtained between simulated and measured results, showing that the proposed PRTS has stable PR in the operation band. Furthermore, owing to the small transversal size of the unit cell compared with the wavelength in the air, the proposed PRTS exhibits angular stability.

II. THEORETICAL ANALYSIS

A. PRTS ELEMENT GEOMETRY

Fig. 1(a) shows the perspective view of one unit cell of the proposed PRTS, which comprises orthogonal PCB pieces with two parallel slotlines arrayed in the vertical direction (x-axis) and another slotline arrayed in the horizontal direction (y-axis). The dielectric substrate of PCB is selected by Rogers 4350B with a relative permittivity of 3.66 and a loss tangent of 0.0037. Fig. 1(b) and Fig. 1(c) show the detailed layouts of the vertical and horizontal slotline structures. It is observed that a pair of parallel-coupled slotline sections (named as Slot1 and Slot2) with short-open ends are etched on the vertical PCB piece and another slotline section (named as Slot3) is etched on the horizontal PCB piece. The three slotline sections can work together to develop the desired co- and cross-polarized transmission paths by coupling Slot1 and Slot2, as well as Slot1 and Slot3, respectively.

B. WORKING PRINCIPLE AND ANALYSIS

The relationship between the electric field and the PR angle is illustrated in Fig. 1(a). The PR angle can be calculated using the following simple equation:

$$\theta = \operatorname{atan}\left(|E_y|/|E_x|\right). \tag{1}$$

From (1), the PR angle θ can be determined by controlling the amplitude ratio of the electric field vectors in the two orthogonal polarizations. Fig. 1(a) also shows a diagrammatic sketch of the simulation setup and electric field

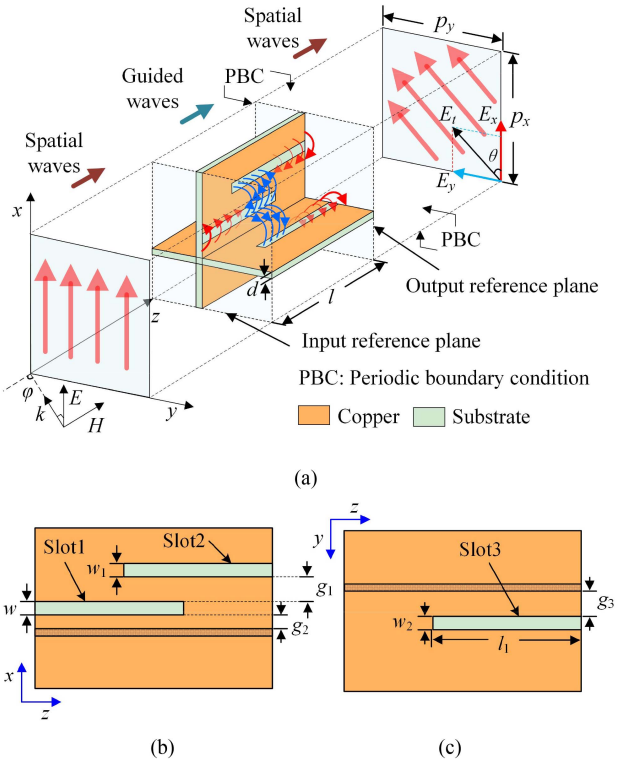

FIGURE 1. Geometry and electric field distribution of the proposed PRTS. (a) Perspective 3-D view of one unit cell with electric field and magnetic field distribution along the slotline. (b) Vertical slotline structure and (c) horizontal slotline structure.

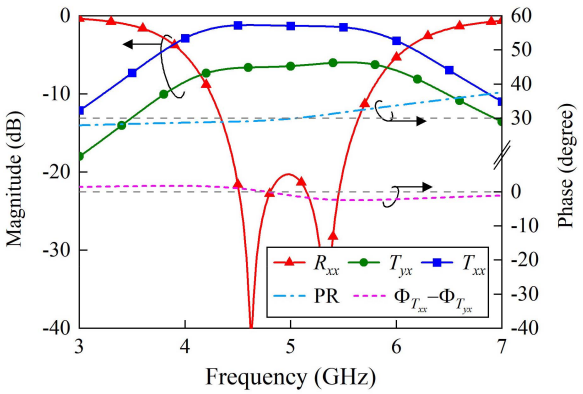

FIGURE 2. Simulated S-parameter results of the proposed PRTS under *x*-polarized incidence. (Physical dimensions (units: mm): $p_x = 10.54$, $p_y = 10.54$, $l = 17.69$, $d = 0.508$, $l_1 = 11.01$, $w = 0.81$, $w_1 = 0.6$, $w_2 = 0.81$, $g_1 = 1.29$, $g_2 = 1.1$, and $g_3 = 1.1$).

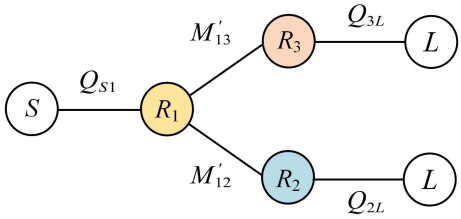

FIGURE 3. Coupling topology of the proposed PRTS element.

distributions of the proposed PRTS, where the red and blue arrows denote the electric and magnetic fields, respectively. When the direction of the electric field is oriented along the *x*-axis, the incident waves are converted into guided waves by the interface between the free space and the open end of Slot1, and then the guided waves are coupled to the two other slotline sections Slot2 and Slot3 by dominant magnetic coupling, respectively. Finally, the guided waves are converted into spatial waves again at the open ends of Slot2 and Slot3. Owing to the controllability of the two orthogonal electric fields along the Slot2 and Slot3, the outgoing electric field can be rotated by a certain angle with respect to those of incidence. To demonstrate the performance of the PRTS, we define $R_{xx} = |E_{rx}|/|E_{ix}|$ and $R_{yx} = |E_{ry}|/|E_{ix}|$ to represent the co- and cross-polarized reflection coefficients, respectively. Similarly, the co- and cross-polarized transmission coefficients are expressed as $T_{xx} = |E_{tx}|/|E_{ix}|$ and $T_{yx} = |E_{ty}|/|E_{ix}|$, respectively. Herein, E_{rx}, E_{ry}, E_{tx}, E_{ty}, and E_{ix} are corresponding to the amplitudes of the co- and cross-polarized reflection waves, co- and cross-polarized transmission waves, and co-polarized incident waves, respectively. Fig. 2 shows the simulated S-parameter results of the proposed PRTS obtained using CST Microwave Studio (CST-MWS) with periodic boundary conditions and Floquet ports. The magnitude of the co-polarized reflection coefficient R_{xx} is less than -20 dB in the operation band. The insertion losses of the co- and cross-polarized transmission coefficients T_{xx} and T_{yx} are approximately -1.27 dB and -6.42 dB, respectively. Therefore, a PR angle of 30° with a slight phase difference can be obtained from 4.5 to 5.5 GHz. It should be mentioned that the cross-polarized reflection coefficient R_{yx} is always kept below -30 dB over the entire frequency band in the simulation, thus it is neglected in the discussion.

To examine the operation principle of the proposed PRTS, a schematic topology can be established, as depicted in Fig. 3, where R_1, R_2, and R_3 denote three resonators with respect to the slotline sections Slot1, Slot2, and Slot3. The spatial waves at both sides of PRS are represented by *S* and *L*, respectively. Besides, the cross- and co-polarized coupling coefficients are denoted by M'_{12} and M'_{13}. The external quality factors are represented by Q_{S1}, Q_{2L}, and Q_{3L}. It is noted that each transmission path is arranged linearly to form a direct coupling path without cross-coupling in selection. This coupling topology can be viewed as a power divider, i.e., a merger of two second-order Chebyshev bandpass filters with a common resonator R_1. To achieve the same RL performance as a real two-port second-order Chebyshev bandpass filter, the coupling coefficients M'_{12} and M'_{13} should satisfy the following equations [36]

$$M'_{12} = \alpha M_{12}, \tag{2}$$
$$M'_{13} = \beta M_{13}, \tag{3}$$

where M_{12} and M_{13} are the coupling coefficients between resonators R_1 and R_2, as well as R_1 and R_3 of an ideal

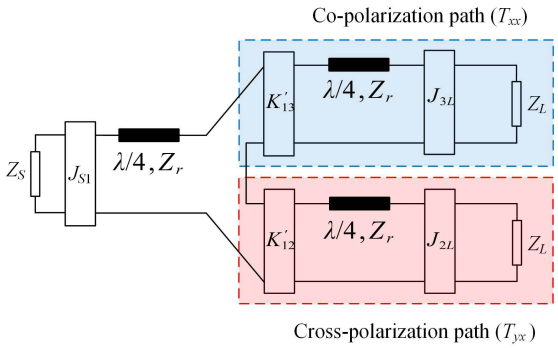

FIGURE 4. Equivalent circuit model of the proposed PRTS element.

two-port second-order Chebyshev bandpass filter, respectively. The coefficients α and β are needed to satisfy the condition of $\alpha^2 + \beta^2 = 1$. Moreover, the three external quality factors of Q_{S1} and Q_{2L}, as well as Q_{3L}, should be equal. Thus, they can be set as Q_e.

Fig. 4 depicts the corresponding equivalent circuit model of the proposed PRTS, where the source and load impedances are denoted by Zs and Z_L, respectively. Herein, Zs and Z_L are equal and thus can be substituted by Z_0. Each resonator developed by the open-short-ended slotline section can be considered a λ/4 resonator. As per the operation mechanism of a λ/4 resonator, it acts either as a shunt LC resonator based on its open-circuit end or a series LC resonator by its short-circuit end [37]. Therefore, the transmission network can be represented by the alternative J and K inverters, as well as λ/4 resonators, which can be calculated as follows:

$$\frac{J_{S1}}{\sqrt{Y_0 Y_r}} = \sqrt{\frac{\pi}{4} \cdot \frac{1}{Q_e}} \tag{4}$$

$$\frac{K_{12}}{Z_r} = \frac{\pi}{4} \cdot M'_{12}, \tag{5}$$

$$\frac{K_{13}}{Z_r} = \frac{\pi}{4} \cdot M'_{13}, \tag{6}$$

where Z_r represents the characteristic impedance of the λ/4 resonator, and the corresponding admittance $Y_r = 1/Z_r$. Y_0 represents wave admittance. It is mentioned that J_{S1}, J_{2L}, and J_{3L} are equal. When the external equation factor Q_e and the coupling coefficients (M'_{12} and M'_{13}) are determined, the theoretical bandpass filter response of the proposed PRTS can be obtained by using (4)–(6).

III. SYNTHESIS PROCEDURE

A. COUPLING MATRIX EXTRACTION

In the coupling topology of Fig. 3, each coupling branch only comprises the main coupling, without cross-coupling or stray coupling. According to the coupled-filter theory, each coupling branch can be easily represented by a coupling matrix, which can be extracted using known specifications, such as center frequency, bandwidth, and RL in the passband [38]. The coupling matrix can be given as follow:

$$\begin{pmatrix} 0 & m_{S1} & 0 & 0 \\ m_{S1} & 0 & m_{12} & 0 \\ 0 & m_{12} & 0 & m_{2L} \\ 0 & 0 & m_{2L} & 0 \end{pmatrix}, \tag{7}$$

where m_{S1} and m_{2L} are the coupling coefficients of the source and load to the corresponding resonators, respectively. m_{12} is the normalization-coupling coefficient between the two coupling resonators. The coupling coefficients between non-adjacent resonators are set to zero because of no cross-couplings. Once the coupling matrix is allotted by the given specifications, the initial values of external quality factor Q_e and coupling coefficient M_{12} can be extracted using the well-known formulas:

$$Q_e = \frac{1}{m_{S1}^2 \cdot \mathrm{FBW}}, \tag{8}$$

$$M_{12} = m_{12} \cdot \mathrm{FBW}, \tag{9}$$

where FBW is the fraction bandwidth. Note that the coupling coefficient M_{12} is an ideal two-port second-order Chebyshev bandpass filter. The coupling coefficient M_{13} is calculated in the same way as that of M_{12}. Based on the above analysis, the parameters Q_e, M_{12}, and M_{13} can be finally achieved by the known specifications. In the meantime, the theoretical response of the proposed PRTS can be obtained as well. The next step in the design procedure is to establish a relationship between the calculated parameters (Q_e, M'_{12}, and M'_{13}) and the physical dimensions of the proposed PRTS.

B. EXTERNAL QUALITY FACTOR Q_E

To extract the external quality factors Q_e, an open-short-ended slotline section is etched on the vertical PCB with periodic boundary conditions under the incidence of x-polarized EM waves, as shown in Fig. 5(a). The incident spatial waves are converted into guided waves by the open end of the slotline section and will be blocked by the short end. Hence, the incident waves will be completely reflected such that the reflection coefficient R_{xx} is almost equal to 0 dB. However, the phase response Φ_{Rxx} distinctly decreases with respect to frequency, as shown in Fig. 5(b). Furthermore, the simulated phase Φ_{Rxx} is equal to zero at the resonant frequency f_0, and the absolute bandwidth between the phase shifts of ±90° is represented by Δf. As per the coupled-resonator theory [39], the extraction of quality factors can be calculated as

$$Q_e = \frac{f_0}{\Delta f_{\pm 90^\circ}}, \tag{10}$$

To examine the sensitivity and effect of the physical dimensions on the external quality factor Q_e and the resonant frequency f_0, a set of parametric studies has been conducted. Fig. 6 shows the external quality Q_e and resonant frequency f_0 versus different values of w, l_1, and g. It can be observed from Fig. 6(a) that the curves of the external quality factor Q_e get reduced by increasing the slotline section width w or the space g. However, the resonant frequency f_0 is slightly affected by the parameters w and g. As shown in Fig. 6(b), the resonant frequency f_0 can be significantly

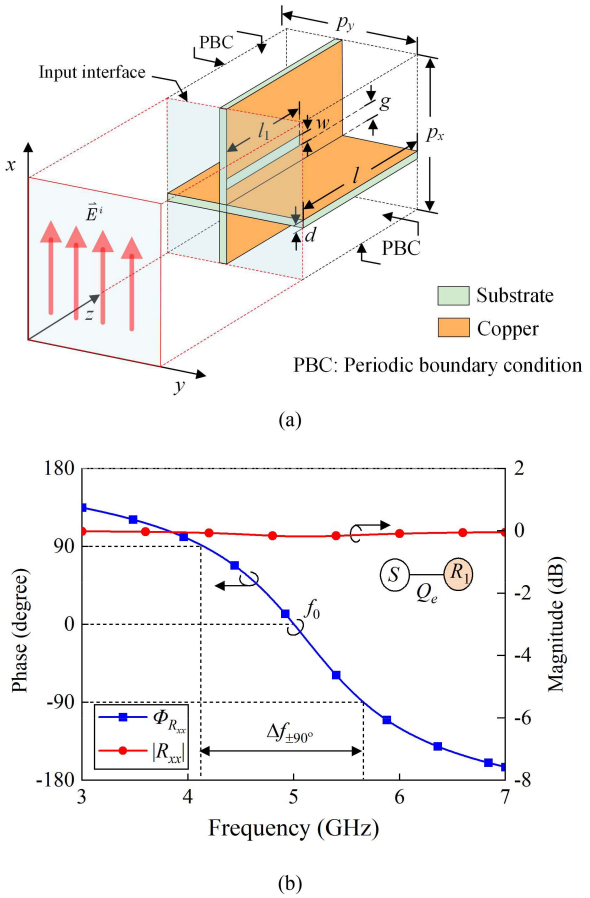

FIGURE 5. Simulation setup and phase response of single slotline section with open-short-end. (a) simulation setup. (b) Phase response and amplitude of R_{xx}. (Physical dimensions (units: mm): $p_x = 10.54$, $p_y = 10.54$, $l = 17.69$, $l_1 = 11.01$, $w = 1.1$, $d = 0.508$, $g = 1.5$).

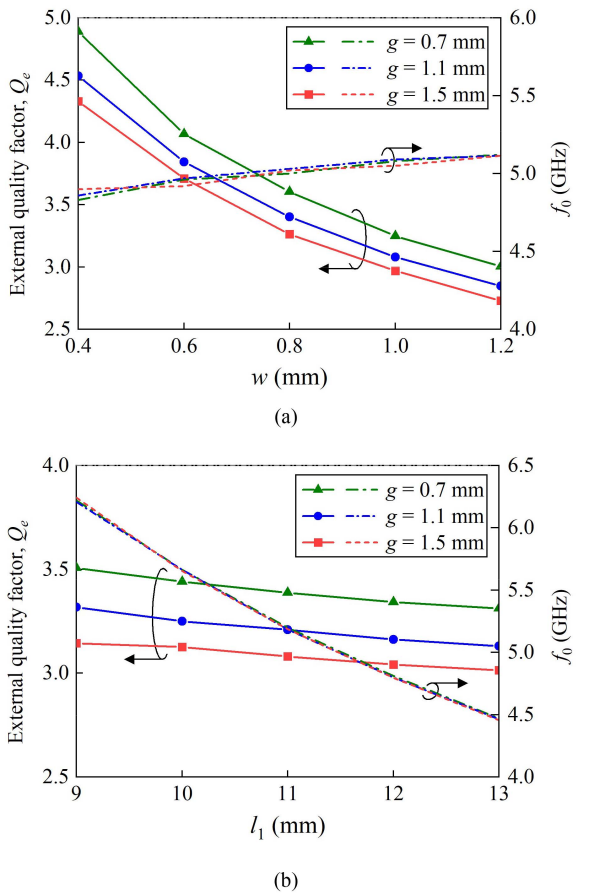

FIGURE 6. Variation of external quality factor Q_e and resonant frequency f_0 with different values of w, l_1, and g. (a) Q_e and f_0 versus w with g. (b) Q_e and f_0 versus l_1 with g. (physical dimensions (units: mm): $p_x = 10.54$, $p_y = 10.54$, $l = 17.69$, and $d = 0.508$).

decreased with increasing l_1, whereas the external quality factor Q_e is slightly decreased with increasing l_1. Hence, it can be well figured out that the desired Q_e can be calculated by the parameters w and g, and the resonant frequency f_0 primarily depends on the slotline section length.

C. COUPLING COEFFICIENTS M'_{12} AND M'_{13}

To obtain the coupling coefficient of the two coupling slotline sections Slot1 and Slot2, the geometry and simulation setup with two slotline sections etched on the orthogonal PCB under x-polarized incidence, as shown in Fig. 7(a). It is observed that two additional metallic layers with rectangular apertures are employed between the PRTS and the free space, respectively. This configuration aims to achieve extremely weak coupling between the source (or load) and the resonators. To eliminate additional effects between the metallic layers and PRTS interfaces, a certain distance (denoted as s) away from the PRTS is required. In this case, the extraction of the coupling coefficient between the two slotline sections is almost unaffected by the port excitation. Note that the rectangular apertures in both metallic layers are selected with a relatively small size to ensure minimal influence on the resonant properties of the resonators. The simulated S-parameter results versus the length of the rectangular aperture l_s are shown in Fig. 7(b), where f_1 and f_2 are the lower and upper resonant frequencies for the two coupling slotline sections. It is seen that a weak port excitation is achieved. The coupling coefficient of the two coupling slotline sections can be calculated using the following formula:

$$M'_{12} = \frac{f_2^2 - f_1^2}{f_2^2 + f_1^2}. \tag{11}$$

To study the relationship between the coupling coefficient M'_{12} and physical dimensions, the variation of the coupling coefficient M'_{12} and resonant frequencies f_1 and f_2 versus the slotline width w, coupling length l_c, and space g are explored. It is worth pointing out that the dimensions of the two slotline sections are the same. As depicted in Fig. 8(a), the two resonant frequencies are almost constant by modifying the slotline width w under each g. Thus, the coupling coefficient M_{12} is not sensitive to the variation of w. As shown in Fig. 8(b), the two resonant frequencies f_1 and f_2 move away from each other by increasing the coupling length l_c or decreasing the space g, resulting in strong coupling. Therefore, the desired coupling coefficient

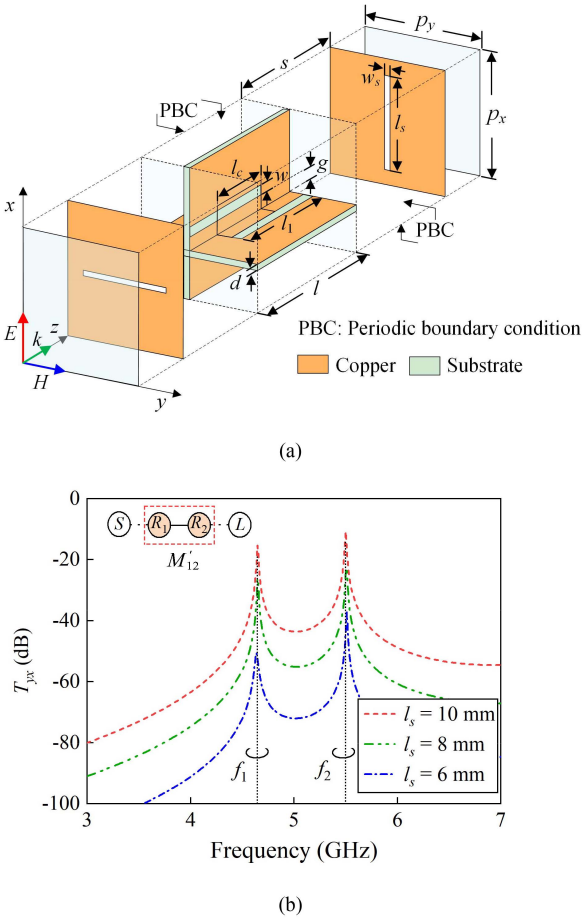

FIGURE 7. (a) Geometry and simulation setup for extracting coupling coefficient M'_{12}. (b) Simulated S-parameter results under x-polarized incidence with respect to different values of l_s. (Physical dimensions (units: mm): $p_x = 10.54$, $p_y = 10.54$, $l = 17.69$, $d = 0.508$, $l_1 = 11.01$, $w = 0.81$, $g = 1.1$, $s = 13$, and $w_s = 0.8$).

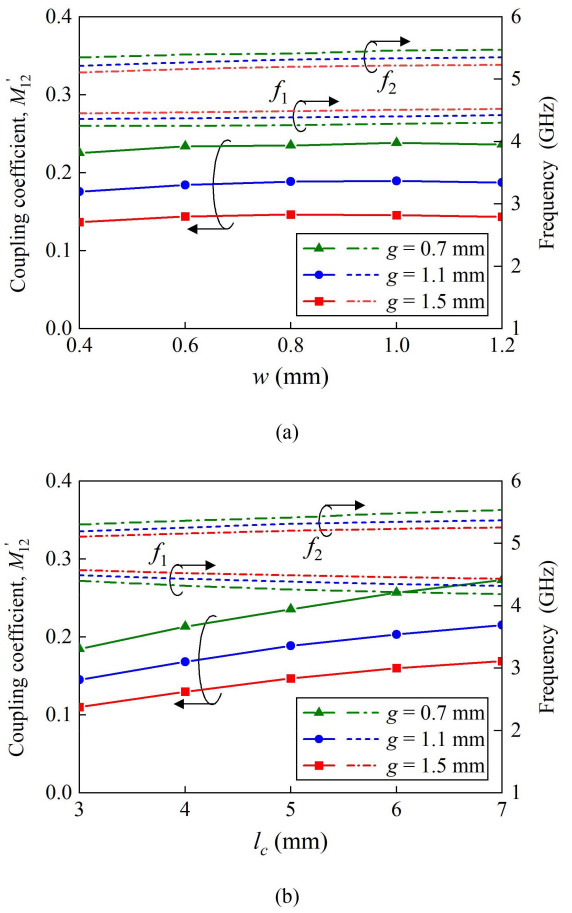

FIGURE 8. Variation of coupling coefficient M'_{12} and resonant frequencies f_1 and f_2 with respect to different values of w, l_c, and g. (a) M'_{12}, f_1 and f_2 with respect to w and g. (b) M'_{12}, f_1 and f_2 with respect to l_c and g. (Physical dimensions (units: mm): $p_x = 10.54$, $p_y = 10.54$, $l = 17.69$, $d = 0.508$, $l_1 = 11.01$, $l_s = 8$, $w_s = 0.8$).

M'_{12} can be primarily realized by adjusting the two parameters l_c and g. Fig. 9 shows the simulation setup to extract the coupling coefficient M'_{13}. The extraction procedure of M'_{13} is the same as that of M'_{12}. The distributions of the coupling coefficient M'_{13}versus the coupling length l_c and slotline width w is shown in Fig. 10. It is seen that M'_{13} increases as increasing the coupling length l_c, while slotline width w has negligible impact on it.

Until now, the theoretical value of the external quality factor Q_e and the ideal coupling coefficients M_{12} and M_{13} have been calculated using the coupled matrix. The practical coupling coefficients M'_{12} and M'_{13} can be calculated and extracted by utilizing (2) and (3). The initial dimensions are then determined by extracting the external quality factor and coupling coefficients. To implement the proposed PRTS as designed by using the above synthesis approach, the entire design procedure can be summarized as follows:

Step 1: Determine the PR angle and the ratio of coupling coefficients, and prescribe the second-order bandpass response, center frequency, bandwidth, and RL.

Step 2: Calculate the coupling matrix using the prescribed parameters [38].

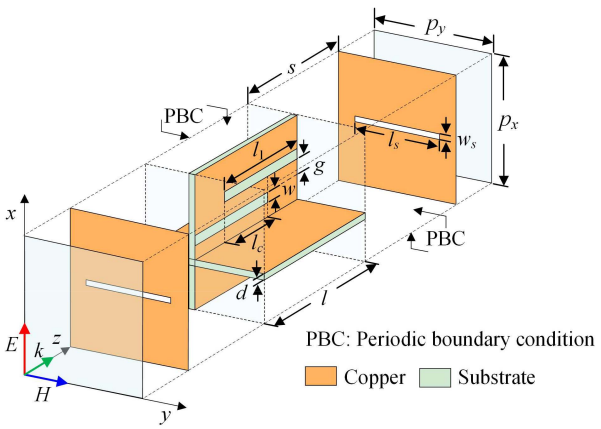

FIGURE 9. Geometry and simulation setup for extracting coupling coefficient M'_{13}.

Step 3: Compute the theoretical values of the external quality factor Q_e and the ideal coupling coefficients M_{12} and M_{13}.

Step 4: Determine the physical dimensions as per the extracted external quality factor Q_e and the two practical coupling coefficients M'_{12} and M'_{13}. Finally, it is necessary to compensate for unexpected effects by slight adjustments,

TABLE 1. Specifications, electrical parameters of the two examples.

	Design example A		Design example B	
Specifications	f_0 = 5 GHz, FBW = 20%, R_{xx} = −20 dB		f_0 = 5 GHz, FBW = 13%, R_{xx} = −20 dB	
PR angle	$\theta = 30^o$	$\theta = 60^o$	$\theta = 30^o$	$\theta = 45^o$
Ratio of coupling coefficient	$\alpha = 1/2$ $\beta = \sqrt{3}/2$	$\alpha = \sqrt{3}/2$ $\beta = 1/2$	$\alpha = 1/2$ $\beta = \sqrt{3}/2$	$\alpha = \sqrt{2}/2$ $\beta = \sqrt{2}/2$
External quality factor and coupling coefficients	$Q_e = 3.34$ $M_{12}^{'} = 0.166$ $M_{13}^{'} = 0.287$	$Q_e = 3.34$ $M_{12}^{'} = 0.287$ $M_{13}^{'} = 0.166$	$Q_e = 5.126$ $M_{12}^{'} = 0.11$ $M_{13}^{'} = 0.187$	$Q_e = 5.126$ $M_{12}^{'} = 0.152$ $M_{13}^{'} = 0.152$
Normalized J/K inverters and characteristic impedance of resonators	$J_{01}/\sqrt{Y_0 Y_r} = 0.4849$ $K_{12}^{'}/Z_r = 0.1304$ $K_{13}^{'}/Z_r = 0.2254$ $Z_r = 130\ \Omega$	$J_{01}/\sqrt{Y_0 Y_r} = 0.4849$ $K_{12}^{'}/Z_r = 0.2254$ $K_{13}^{'}/Z_r = 0.1304$ $Z_r = 130\ \Omega$	$J_{01}/\sqrt{Y_0 Y_r} = 0.3914$ $K_{12}^{'}/Z_r = 0.0863$ $K_{13}^{'}/Z_r = 0.1469$ $Z_r = 100\ \Omega$	$J_{01}/\sqrt{Y_0 Y_r} = 0.3914$ $K_{12}^{'}/Z_r = 0.1194$ $K_{13}^{'}/Z_r = 0.1194$ $Z_r = 96.7\ \Omega$

TABLE 2. The physical dimensions of the two examples.

	Parameters (units: mm)	p_x	p_y	l	d	l_1	w	w_1	w_2	g_1	g_2	g_3
Example A	PR angle $\theta = 30^o$	10.45	10.54	17.69	0.508	11.01	0.81	0.6	0.81	1.29	1.1	1.1
	PR angle $\theta = 60^o$	10	10	16.58	0.508	11.2	1.07	0.88	0.97	4.4	0.37	0.37
Example B	PR angle $\theta = 30^o$	10.55	10.29	17	0.508	10.38	0.31	0.19	0.3	2	0.63	1.98
	PR angle $\theta = 45^o$	10.82	10.28	17.3	0.508	10.85	0.25	0.23	0.24	2.57	0.96	0.96

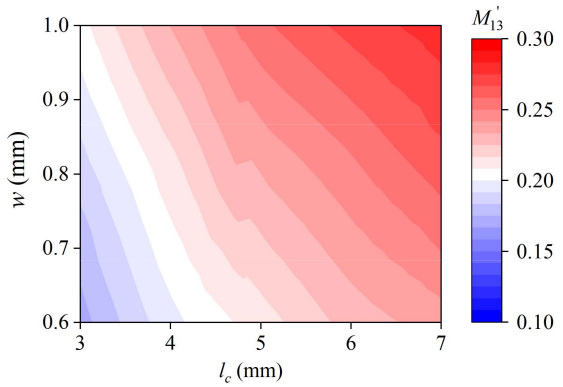

FIGURE 10. Distributions of coupling coefficient $M_{13}^{'}$ with respect to different values of w, l_c. (Physical dimensions (units: mm): p_x = 10.54, p_y = 10.54, l = 17.69, d = 0.508, l_1 = 11.01, w_s = 0.8, l_s = 10, and g = 2.5).

so as to ensure that the desired PR angle and the frequency response meet the design requirements.

IV. EXPERIMENTAL VERIFICATION AND DISCUSSION

A. THEORETICAL DESIGN EXAMPLES

Two examples with second-order Chebyshev filtering response and different FBWs (20% and 13%) at the same center frequency of f_0 = 5 GHz and RL of 20 dB are designed to confirm the synthesis procedure of the proposed PRTS. Example A is designed to realize the PR angles of 30° and 60°, and example B can achieve the PR angles of 30° and 45°. The calculated parameters are listed in Table 1, and the corresponding physical dimensions are presented in Table 2.

It is worth mentioning that the coefficients of the coupling matrix of the two examples are equal to each other, i.e., $m_{S1} = 1.225$, $m_{12} = 1.658$, $m_{2L} = 1.225$. Besides,

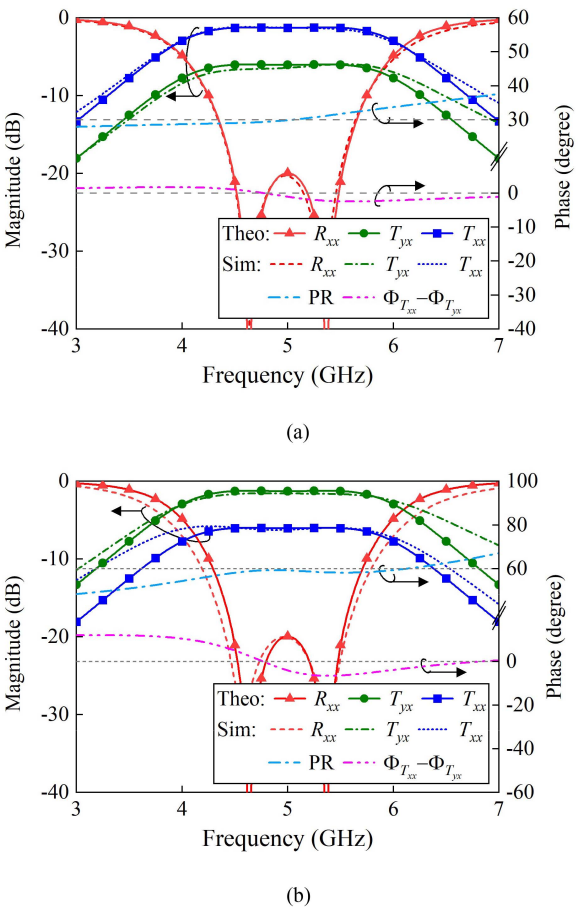

FIGURE 11. Comparison of theoretical response from the equivalent circuit model and the EM-simulated results of example A shown in Fig. 1(a). (a) PR angle of 30° and (b) PR angle of 60°.

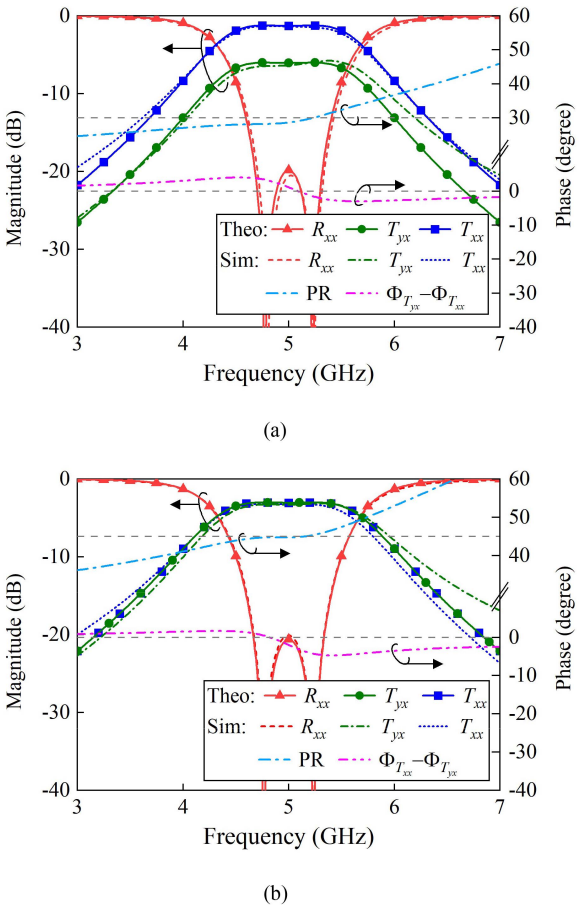

FIGURE 12. Comparison of theoretical response from the equivalent circuit model and the EM-simulated results of example B shown in Fig. 1(a). (a) PR angle of 30° and (b) PR angle of 45°.

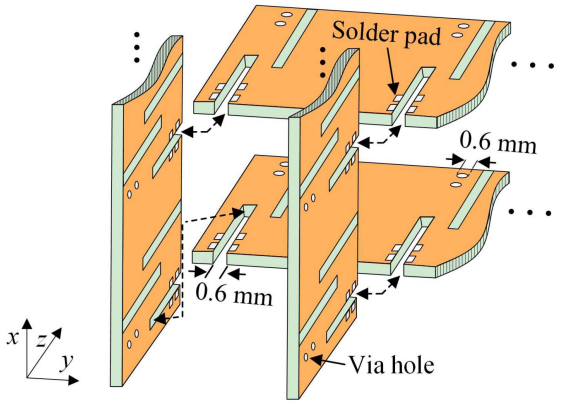

FIGURE 13. Assembly details of the proposed PRTS.

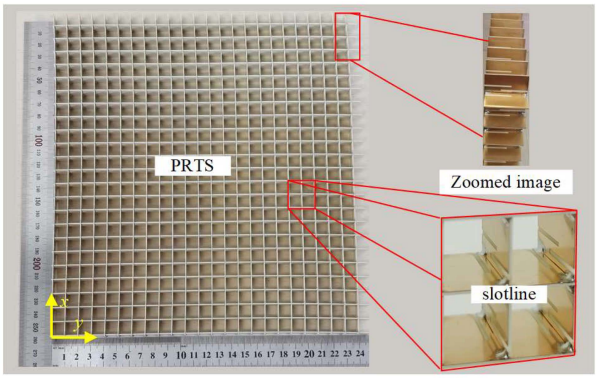

FIGURE 14. Photograph of the fabricated PRTS prototype.

the port impedance is $Z_0 = 377\ \Omega$. The S-parameters and PR comparisons between the theoretical results achieved by the equivalent circuit model and the full-wave EM simulation results obtained in CST-MWS of example A is shown in Fig. 11. As is observed in Fig. 11(a) and Fig. 11(b), two PR angles of 30° and 60° can be realized over the frequency range of 4.5 – 5.5 GHz, and the simulated phase differences, $\Delta\Phi = \Phi_{Txx} - \Phi_{Tyx}$, of the two transmission paths are less than $0° \pm 2.3°$ and $0° \pm 6°$ compared to theoretical ones, respectively. The small discrepancies in the phase difference are possible because the two transmission paths are not exactly symmetrical in the unit cell. For design example B, a PR angle of 30° with a maximum phase deviation of $0° \pm 3.5°$ is obtained, as shown in Fig. 12(a). Fig. 12(b) shows that the phase difference $\Delta\Phi$ under the PR angle is set to 45°. It is seen that $\Delta\Phi$ is less than $0° \pm 4.5°$. The reflection coefficients R_{xx} of the two examples are below −20 dB over the operation band. The simulation results are displayed to confirm the feasibility of the design concept.

B. FABRICATION AND MEASUREMENT

Prototypes A and B with PR angles of 30° and 45° are then fabricated and measured, respectively. Fig. 13 shows the assembly details of our design, where two narrow slits are cut half away along vertical and horizontal PCBs, respectively. In this case, the vertical and horizontal PCBs can be cross-joined to realize an entire structure using the cut slits. To ensure all the PCBs are fixed together, several vias and solder pads are added at the two sides of the PCBs. It should be noted that the performance of the PRTS is not affected by the added vias and solder pads. The PRTS prototypes were fabricated using Rogers 4350B substrate with a thickness of 0.508 mm. Fig. 14 shows the structural details of prototype A, where each PCB piece has 23 periodic unit cells, i.e., 23 × 23 elements are established and the total dimension is 250 mm × 250 mm, which corresponds to the electrical dimensions of $4.2\lambda_0 \times 4.2\lambda_0$, where λ_0 represents the free-space wavelength at the center frequency. The magnified views of the four elements and the side view of the proposed PRTS show the relative location of the three coupling slotline sections and the details of the structure.

Fig. 15 shows an image of the measurement scheme. The measurement system is set up in a free-space microwave anechoic chamber, which is composed of transmitting and receiving horn antennas, the measured prototype, and a vector network analyzer. In this measurement system, the two horn antennas should be kept at a certain distance (d) away from the test screen to satisfy the far-field distance requirement of the antennas, i.e., $d > 2D^2/\lambda$, where D is the largest dimension of the antenna and λ is the wavelength of the highest operation frequency. The measured prototype was

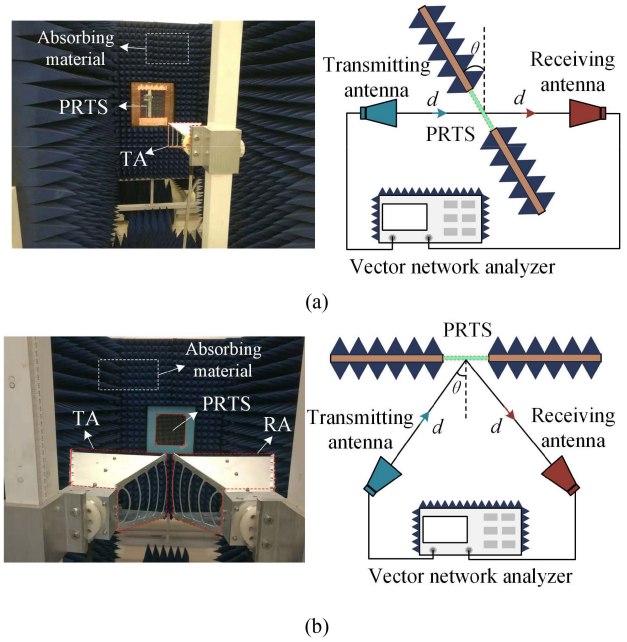

FIGURE 15. Photographs of measurement setups. (a) Transmission measurement and (b) reflection measurement.

centrally positioned on a foam block. Except for minor differences in assembly, the measurement procedures of these two prototypes are similar. To obtain accurate measurement results, the measurement procedure of the PRTS is conducted in two primary steps: First, the air box and the perfect electric conductor (PEC) with the same dimension as the proposed PRTS structure are measured without the proposed PRTS. These measurements are used to calibrate the measured PRTS data. Then, the PRTS structure is measured. Finally, by normalizing the measured results to the calibration data with the help of MATLAB, the frequency response of PRTS can be obtained.

C. RESULTS AND DISCUSSIONS

The simulation and measurement results of these two designed prototypes at incident angles of 0°, 20°, and 40° are compared in Fig. 16 and Fig. 17, respectively. As shown in Fig. 16(a) and Fig. 17(a), the measured T_{yx}, T_{xx}, and R_{xx} are in good agreement with the simulated ones. Moreover, under the normal incidence, co-polarized reflection coefficients R_{xx} of the two prototypes are less than −18 dB over the operation band ranges of 4.5–5.5 and 4.675–5.325 GHz, respectively. Meanwhile, the measured PR angles are within 30° ± 1.3° and 45° ± 1.5°, respectively. The differences in PR angles between the simulation and measurement results are less than 3° for both examples. The differences are possibly attributed to fabrication tolerance, dielectric substrate deformation, and uncertainties in the measurement setup unaccounted for in the simulation model. The measured PR angles are within 30° ± 1.8° and 45° ± 3° compared to simulated results when the oblique incident angle is increased to 20°, as shown in Fig. 16(b) and Fig. 17(b). As shown in Fig. 16(c) and 17(c), the PR angles are still relatively stable with oblique incidence

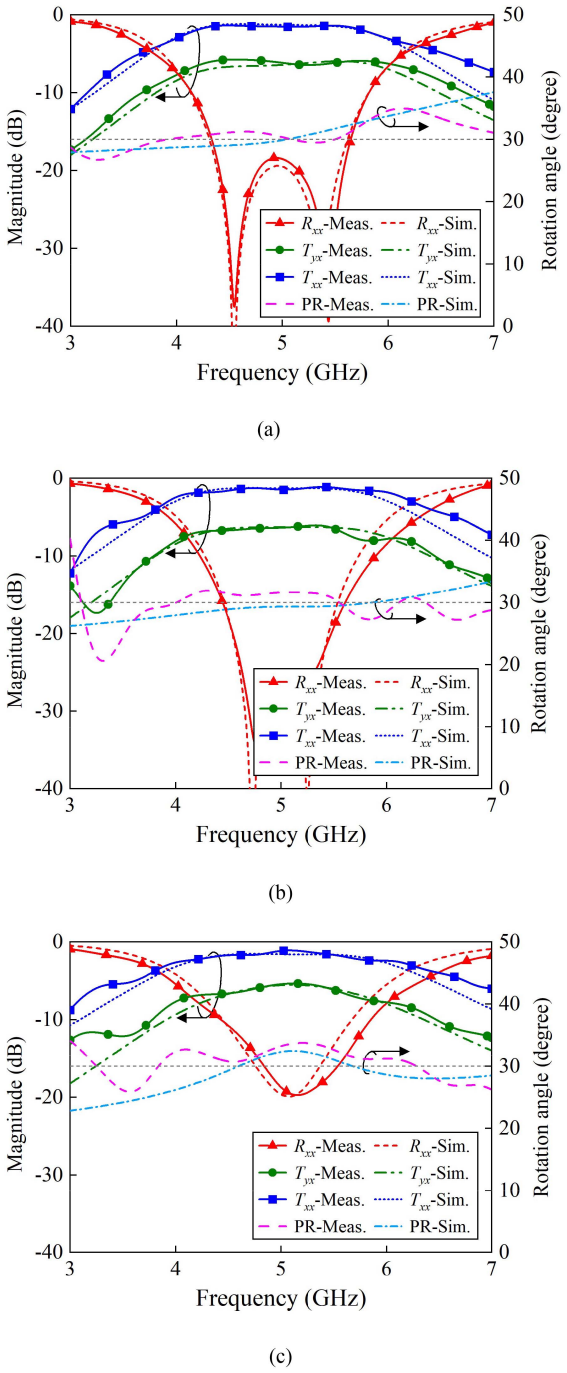

FIGURE 16. Measured and simulated S-parameter results, as well as PR angle $\theta = 30°$ of the fabricated example A at different incident angles of $\varphi = 0°$, 20°, and 40°. (a) Oblique incident angle $\varphi = 0°$. (b) Oblique incident angle $\varphi = 20°$ and (c) oblique incident angle $\varphi = 40°$.

up to 40°. In order to show the total energy transmission efficiency (ETE) of the two orthogonal branches, a simple formula is given as follows:

$$\mathrm{ETE} = \left(|T_{xx}|^2 + |T_{yx}|^2\right) / \left(|T_{xx}|^2 + |T_{yx}|^2 + |R_{xx}|^2\right). \quad (12)$$

The simulated and measured ETE of the two orthogonal branches are shown in Fig. 18(a) and Fig. 18(b). It is observed that the measured ETE of the two examples A

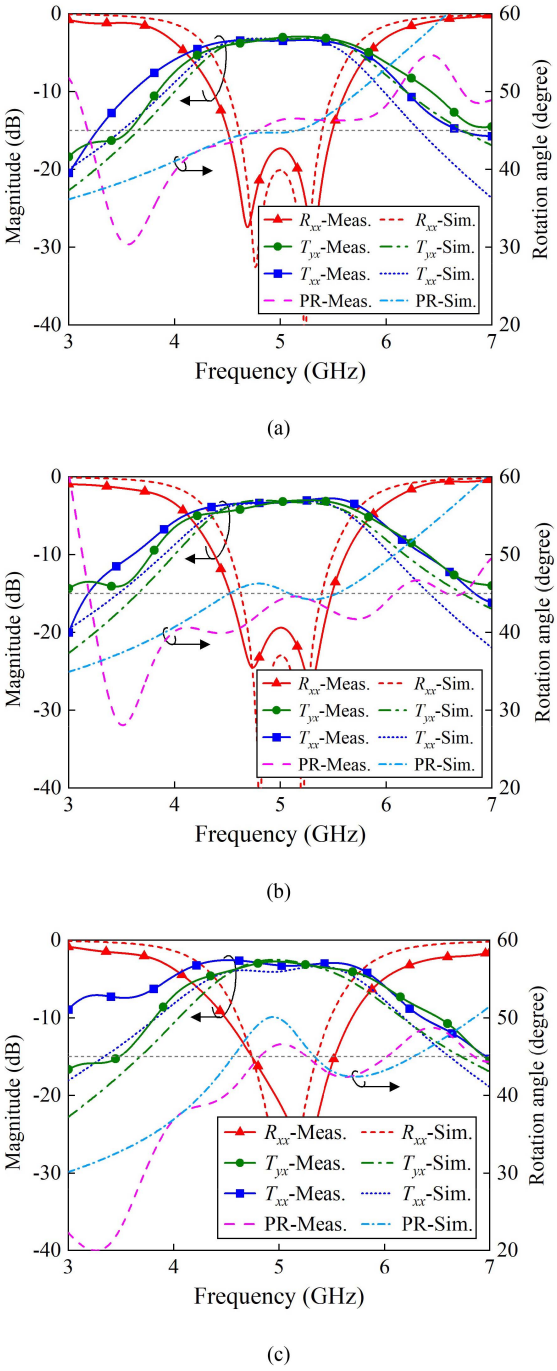

FIGURE 17. Measured and simulated S-parameter results, as well as PR angle $\theta = 45°$ of the fabricated example B at different incident angles of $\varphi = 0°$, 20°, and 40°. (a) Oblique incident angle $\varphi = 0°$. (b) Oblique incident angle $\varphi = 20°$ and (c) oblique incident angle $\varphi = 40°$.

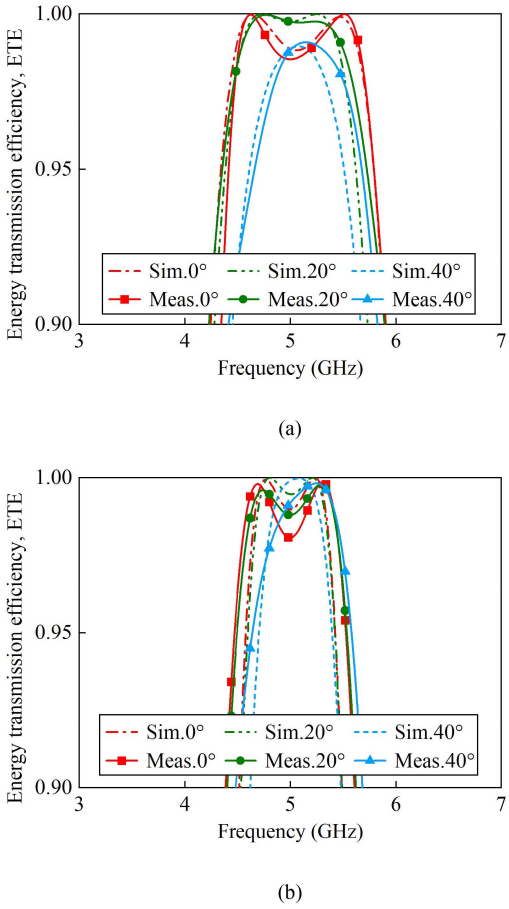

FIGURE 18. Simulated and measured transmission efficiency under different incident angles of $\varphi = 0°$, 20°, and 40°. (a) Example A and (b) example B.

and B can be up to 98.8% and 99% under the normal incidence, respectively. As the oblique incident angle $\varphi = 40°$, the total of the measured ETE of both examples is still above 98% in the operation band. It implies that almost all of the energy can be transmitted through the PRTS by the orthogonal coupling slotlines.

A comparison between our designs with other PR surfaces in the literature is presented in Table 3. It reveals that although the profile of the proposed PRTS is thicker than other designs, our proposed design can achieve a smaller size of each unit cell in transversal cross-section than others and thus it has a larger oblique incident angle than others. More importantly, our proposed design can be synthesized using the coupling matrix, which can remarkably improve design efficiency and provide greater flexibility.

V. CONCLUSION

In this article, a novel PRTS of arbitrary angle based on 3-D FSSs is proposed, which is developed using three parallel-coupled slotline sections with open-short ends etched on two orthogonal dielectric substrates. The three slotline sections can form two orthogonal transmission paths. The polarization of the outgoing EM waves can be determined by the ratio of the coupling coefficient of each path. To reveal the operating mechanism, a filtering power divider concept and an equivalent circuit model are employed to analyze first, and a synthesis scheme based on the coupling matrix is utilized to synthesize and design the proposed PRTS. To validate the design concept, two examples with different FBWs and PR

TABLE 3. Comparisons of our proposed PRTSs and other designs in the literature.

Ref.	2-D/3-D (unit cell)	Thickness (λ_0)	Unit size (λ_0)	Relative bandwidth (normal incidence)	PR angle	Angular stability	Synthesis
[2]	2-D (Double layers)	0.053 (ε_r=2.2)	0.28	9.76–10.57 GHz (8%) ($\|S_{11}\| < -10$ dB)	Only 90°	30°	No
[15]	2-D (Three layers)	0.078 (ε_r=2.65)	0.35	5.68-5.92 GHz (4%) ($\|S_{11}\| < -10$ dB)	Only 90°	45°	No
[23]	2-D (Five layers)	0.013 (ε_r=3.55)	0.27	4.78–5.2 GHz (8.8%) ($\|S_{11}\| < -15$ dB)	Only 90°	50°	No
[25]	2-D (Double layers)	0.84	0.66	21.4–22.4 GHz (4.5%) ($\|S_{11}\| < -20$ dB)	30°	—	No
[27]	2.5-D (Double layers)	0.053 (ε_r=2.2)	0.49	34.3–36.5 GHz (6.2%) ($\|S_{11}\| < -10$ dB)	45°	—	No
[28]	2.5-D (Double layers)	0.18 (ε_r=2.2)	0.49	31.7–38.3 GHz (18.8%) ($\|S_{11}\| < -10$ dB)	90°	—	No
Example A	3-D (Single layer)	0.29 (ε_r=3.66)	0.17	4.5–5.5 GHz (20%) ($R_{xx} < -20$ dB)	30°	40°	Yes
Example B	3-D (Single layer)	0.29 (ε_r=3.66)	0.18	4.675–5.325 GHz (13%) ($R_{xx} < -20$ dB)	45°	40°	Yes

λ_0: the free-space wavelength at the center frequency.

angles at the same center frequency and RL are developed. Finally, two PRTS prototypes with PR angles of 30° and 45° are fabricated and measured, respectively. The measured results agree well with the theoretical and simulated results, thus verifying that the proposed PRTS exhibits good stability under a large incident angle.

REFERENCES

[1] Y. Liu, Y. Hao, K. Li, and S. Gong, "Radar cross section reduction of a microstrip antenna based on polarization conversion metamaterial," *IEEE Antennas Wireless Propag. Lett.*, vol. 15, pp. 80–83, 2016.

[2] M. Saikia, S. Ghosh, and K. V. Srivastava, "Design and analysis of ultrathin polarization rotating frequency selective surface using V-shaped slots," *IEEE Antennas Wireless Propag. Lett.*, vol. 16, pp. 2022–2025, 2017.

[3] F. Wang, K. Li, and Y. Ren, "Reconfigurable polarization rotation surfaces applied to the wideband antenna radar cross section reduction," *Int. J. RF Microw. Comput. Eng.*, vol. 28, no. 5, Jun. 2018, Art. no. e21262.

[4] S. Sun, W. Jiang, S. Gong, and T. Hong, "Reconfigurable linear-to-linear polarization conversion metasurface based on PIN diodes," *IEEE Antennas Wireless Propag. Lett.*, vol. 17, no. 9, pp. 1722–1726, Sep. 2018.

[5] R. Zaker and A. Sadeghzadeh, "A low-profile design of polarization rotation reflective surface for wideband RCS reduction," *IEEE Antennas Wireless Propag. Lett.*, vol. 18, no. 9, pp. 1794–1798, Sep. 2019.

[6] S. Sun, W. Jiang, X. Li, P. Liu, and S. Gong, "Ultrawideband high-efficiency 2.5-dimensional polarization conversion metasurface and its application in RCS reduction of antenna," *IEEE Antennas Wireless Propag. Lett.*, vol. 18, no. 5, pp. 881–885, May 2019.

[7] A. A. Omar, W. Hong, A. Al-Awamry, and A. E. Mahmoud, "A single-layer vialess wideband reflective polarization rotator utilizing perforated holes," *IEEE Antennas Wireless Propag. Lett.*, vol. 19, no. 12, pp. 2053–2056, Dec. 2020.

[8] T. Freialdenhoven, T. Bertuch, S. Stanko, D. Nötel, D. I. L. Vorst, and T. Dallmann, "Design of a polarization rotating SIW-based reflector for polarimetric radar application," *IEEE Trans. Antennas Propag.*, vol. 68, no. 11, pp. 7414–7422, Nov. 2020.

[9] M. Cerveny, K. L. Ford, and A. Tennant, "Reflective switchable polarization rotator based on metasurface with PIN diodes," *IEEE Trans. Antennas Propag.*, vol. 69, no. 3, pp. 1483–1492, Mar. 2021.

[10] J. Wang, Z. Shen, and W. Wu, "Cavity-based high-efficiency and wideband 90° polarization rotator," *Appl. Phys. Lett.*, vol. 109, no. 15, Oct. 2016, Art. no. 153504.

[11] K. K. Varikuntla and R. Singaravelu, "Ultrathin design and implementation of planar and conformal polarisation rotating frequency selective surface based on SIW technology," *IET Microw. Antennas Propag.*, vol. 12, no. 12, pp. 1939–1947, Oct. 2018.

[12] E. Arnieri, F. Greco, L. Boccia, and G. Amendola, "A SIW-based polarization rotator with an application to linear-to-circular dual-band polarizers at K-/Ka-band," *IEEE Trans. Antennas Propag.*, vol. 68, no. 5, pp. 3730–3738, May 2020.

[13] J. Feng, H. Shi, J. Yi, A. Zhang, and Z. Xu, "Band-pass filtering cross-polarization converter using transmitarrays," *Materials*, vol. 14, no. 9, p. 2109, Apr. 2021.

[14] X. Liu, T. Qi, C. Wang, X. Yang, L. Gan, and Q. Cai, "A broadband ultra-thin polarization rotator using periodically loaded parallel strip-lines," *IEEE Access*, vol. 9, pp. 25450–25457, 2021.

[15] S. Y. Wang, J. D. Bi, W. Liu, W. Geyi, and S. Gao, "Polarization-insensitive cross-polarization converter," *IEEE Trans. Antennas Propag.*, vol. 69, no. 8, pp. 4670–4680, Aug. 2021.

[16] X. Gao, L. Singh, W. Yang, J. Zheng, H. Li, and W. Zhang, "Bandwidth broadening of a linear polarization converter by near-field metasurface coupling," *Sci. Rep.*, vol. 7, no. 1, pp. 1–8, 2017.

[17] A. A. Omar, A. Mahmoud, J. Choi, and W. Hong, "Wideband transmissive polarization rotator with in-band notches enabling multiband operation," *IEEE Access*, vol. 9, pp. 44751–44756, 2021.

[18] S. A. Winkler, W. Hong, M. Bozzi, and K. Wu, "Polarization rotating frequency selective surface based on substrate integrated waveguide technology," *IEEE Trans. Antennas Propag.*, vol. 58, no. 4, pp. 1202–1213, Apr. 2010.

[19] Y. Zuo, Z. X. Shen, and Y. J. Feng, "Frequency-selective microwave polarization rotator using substrate-integrated waveguide cavities," *Chin. Phys. B*, vol. 23, no. 3, Mar. 2014, Art. no. 034101.

[20] X. C. Zhu et al., "Design of a bandwidth-enhanced polarization rotating frequency selective surface," *IEEE Trans. Antennas Propag.*, vol. 62, no. 2, pp. 940–944, Feb. 2014.

[21] Y. Zhang, J. Z. Zhu, C. P. Huang, and S. J. Ma, "Wide-band and high-efficiency 90° polarization rotator based on tri-layered perforated metal films," *J. Lightw. Technol.*, vol. 35, no. 21, pp. 4817–4823, Nov. 1, 2017.

[22] N. M. Littman, S. G. O'Keefe, A. Galehdar, H. G. Espinosa, and D. V. Thiel, "Ultra-thin broadband transmission FSS for linear polarization rotation," *IEEE Access*, vol. 9, pp. 127335–127342, 2021.

[23] J. M. Xie, B. Li, L. Zhu, and H. Li, "High-order bandpass polarization rotator based on aperture-coupled patch resonators," *IEEE Antennas Wireless Propag. Lett.*, vol. 20, no. 9, pp. 1809–1813, Sep. 2021.

[24] T. K. Wu, "Meander-line polarizer for arbitrary rotation of linear polarization," *IEEE Microw. Guided Wave Lett.*, vol. 4, no. 6, pp. 199–201, Jun. 1994.

[25] X. Liu et al., "Polarization rotator of arbitrary angle based on simple slot-array," *AIP Adv.*, vol. 5, no. 12, 2015, Art. no. 127142.

[26] N. Kolmakova, S. Prikolotin, A. Perov, V. Derkach, and A. A. Kirilenko, "Polarization plane rotation by arbitrary angle using symmetrical structures," *IEEE Trans. Microw. Theory Techn.*, vol. 64, no. 2, pp. 429–435, Feb. 2016.

[27] M. S. M. Mollaei, "Narrowband configurable polarization rotator using frequency selective surface based on circular substrate-integrated waveguide cavity," *IEEE Antennas Wireless Propag. Lett.*, vol. 16, pp. 1923–1926, 2017.

[28] M. S. M. Mollaei, E. Zanganeh, R. Heydarian, F. R. Rostami, and S. M. Pourangha, "Broadband polarization rotator for arbitrary angles with enhanced substrate integrated waveguide cavities," *Int. J. RF Microw. Comput. Eng.*, vol. 28, no. 8, Oct. 2018, Art. no. e21407.
[29] A. K. Rashid and Z. Shen, "A novel band-reject frequency selective surface with pseudo-elliptic response," *IEEE Trans. Antennas Propag.*, vol. 58, no. 4, pp. 1220–1226, Apr. 2010.
[30] A. K. Rashid and Z. Shen, "Scattering by a two-dimensional periodic array of vertically placed microstrip lines," *IEEE Trans. Antennas Propag.*, vol. 59, no. 7, pp. 2599–2606, Jul. 2011.
[31] B. Li and Z. Shen, "Dual-band bandpass frequency-selective structures with arbitrary band ratios," *IEEE Trans. Antennas Propag.*, vol. 62, no. 11, pp. 5504–5512, Nov. 2014.
[32] H. Li, B. Li, and L. Zhu, "Wideband bandpass frequency-selective structures on stacked slotline resonators: Proposal and synthetic design," *IEEE Trans. Antennas Propag.*, vol. 68, no. 10, pp. 7068–7078, Oct. 2020.
[33] G. Q. Luo, W. Yu, Y. Yu, X. H. Zhang, and Z. Shen, "A three-dimensional design of ultra-wideband microwave absorbers," *IEEE Trans. Microw. Theory Techn.*, vol. 68, no. 10, pp. 4206–4215, Oct. 2020.
[34] L. Zhou and Z. Shen, "3-D absorptive energy-selective structures," *IEEE Trans. Antennas Propag.*, vol. 69, no. 9, pp. 5664–5672, Sep. 2021.
[35] J. Zhu, W. Gao, Y. Shi, W. Li, and W. Tang, "A dual-polarized bandpass frequency selective surface with stable response," *IEEE Antennas Wireless Propag. Lett.*, vol. 20, no. 5, pp. 673–677, May 2021.
[36] C. F. Chen, J. J. Li, G. Y. Wang, K. W. Zhou, and R. Y. Chen, "Design of compact filtering 180-degree hybrids with arbitrary power division and filtering response," *IEEE Access*, vol. 7, pp. 18521–18530, 2019.
[37] S. Zhang and L. Zhu, "Synthesis method for even-order symmetrical Chebyshev bandpass filters with alternative J/K inverters and λ/4 resonators," *IEEE Trans. Microw. Theory Techn.*, vol. 61, no. 2, pp. 808–816, Feb. 2013.
[38] R. J. Cameron, "Advanced coupling matrix synthesis techniques for microwave filters," *IEEE Trans. Microw. Theory Techn.*, vol. 51, no. 1, pp. 1–10, Jan. 2003.
[39] J.-S. Hong and M. J. Lancaster, *Microstrip Filters for RF/Microwave Applications*, 2nd ed. Hoboken, NJ, USA: Wiley, 2011.

TAO WEI (Graduate Student Member, IEEE) received the B.S. and M.S. degrees from Guangxi Normal University, Guilin, China, in 2009 and 2014, respectively. He is currently pursuing the Ph.D. degree with the Nanjing University of Posts and Telecommunications, Nanjing, China.

Since 2014, He has been a Lecturer with the School of Information Engineering, Baise University. His current research interests include frequency selective surfaces, polarization rotation surfaces, and phased array antennas.

BO LI (Senior Member, IEEE) received the B.S. and Ph.D. degrees in communication engineering from the Nanjing University of Science and Technology, China, in 2006 and 2011, respectively.

From November 2011 to May 2014, he was with Nanyang Technological University, Singapore, as a Research Fellow. In June 2014, he joined the Nanjing University of Posts and Telecommunications, China, where he has been a Full Professor since July 2015. He was a Postdoctoral Fellow with the Faculty of Science and Technology, University of Macau, China, from July 2017 to January 2018 and from September 2019 to March 2020, and a Visiting Professor with the State Key Laboratory of Terahertz and Millimeter Waves, City University of Hong Kong, China, from January to April 2018. He has authored or coauthored more than 90 papers in international journals and conference proceedings. His research interests include RF/microwave circuits and frequency-selective surfaces.

Prof. Li received the Young Scientist Award of 2019 PIERS in Xiamen, China.

HANXUAN LI (Graduate Student Member, IEEE) was born in Yangzhou, Jiangsu, China, in 1994. He received the B.Eng. and Ph.D. degrees from the Nanjing University of Posts and Telecommunications, Nanjing, China, in 2016 and 2022, respectively.

His current research interests include the design of frequency selective surfaces and antennas for microwave and millimeter-wave applications.

LEI ZHU (Fellow, IEEE) received the B.Eng. and M.Eng. degrees in radio engineering from the Nanjing Institute of Technology (currently Southeast University), Nanjing, China, in 1985 and 1988, respectively, and the Ph.D. degree in electronic engineering from the University of Electro-Communications, Tokyo, Japan, in 1993.

He was a Research Engineer with Matsushita-Kotobuki Electronics Industries Ltd., Tokyo, from 1993 to 1996, a Research Fellow with the École Polytechnique de Montréal, Montréal, QC, Canada, from 1996 to 2000, and an Associate Professor with the School of Electrical and Electronic Engineering, Nanyang Technological University, Singapore, from 2000 to 2013. He joined the Faculty of Science and Technology, University of Macau, Macau, China, as a Full Professor in August 2013, and has been a Distinguished Professor since December 2016. From August 2014 to August 2017, he served as the Head of Department of Electrical and Computer Engineering, University of Macau. So far, he has authored or coauthored more than 725 papers in international journals and conference proceedings. His papers have been cited more than 14 000 times with the H-index of 58 (source: Scopus). His research interests include microwave circuits, antennas, periodic structures, and computational electromagnetics.

Dr. Zhu was the recipient of the 1993 Achievement Award in Science and Technology (First Prize) from the National Education Committee of China, the 1996 Silver Award of Excellent Invention from Matsushita-Kotobuki Electronics Industries Ltd., the 1997 Asia–Pacific Microwave Prize Award, the 2020 FST Research Excellence Award from the University of Macau, and the 2020 and 2022 Macao Natural Science Awards (Second Prize) from the Science and Technology Development Fund, Macau. He was an Associate Editor for the IEEE TRANSACTIONS ON MICROWAVE THEORY AND TECHNIQUES from 2010 to 2013 and IEEE MICROWAVE AND WIRELESS COMPONENTS LETTERS from 2006 to 2012. He served as the General Chair for the 2008 IEEE MTT-S International Microwave Workshop Series on the Art of Miniaturizing RF and Microwave Passive Components, Chengdu, China, and a Technical Program Committee Co-Chair of the 2009 Asia–Pacific Microwave Conference, Singapore. He served as the member of IEEE MTT-S Fellow Evaluation Committee from 2013 to 2015, and as the member of IEEE AP-S Fellows Committee from 2015 to 2017.

CHONG-HU CHENG (Member, IEEE) received the B.S., M.S., and Ph.D. degrees in electronic science and engineering from Southeast University, Nanjing, China, in 1983, 1986, and 1993, respectively. From 1994 to 1996, he was a Postdoctoral Researcher with the Department of Information Electronics, Zhejiang University, China. From 1996 to 1999, he served as a Lecturer with Hainan University, China. From 1999 to 2001, he was a Research Fellow with the National Institute of Information and Communications Technology, Japan. He joined the College of Telecommunications and Information Engineering, Nanjing University of Posts and Telecommunications, as an Associate Professor in 2001, and became a Full Professor in 2006. He has authored or coauthored more than 100 technical publications. His research interests include computational electromagnetics, small antennas, and microwave passive circuits. He served as a Reviewer for several international journals, including the IEEE MICROWAVE AND WIRELESS COMPONENT LETTERS and IET ELECTRONICS LETTERS. He is a member of the China Institute of Electronics, Antenna Society.